Brain Structure and Function (2018) 223:1001–1015
https://doi.org/10.1007/s00429-017-1595-8

METHODS PAPER

Analysis of the vasculature by immunohistochemistry in paraffin-embedded brains

Yann Decker[1,2] · Andreas Müller[3] · Eszter Németh[1,2] · Walter J. Schulz-Schaeffer[4] · Marc Fatar[5] · Michael D. Menger[6] · Yang Liu[1,2] · Klaus Fassbender[1,2]

Received: 31 May 2017 / Accepted: 12 December 2017 / Published online: 19 December 2017

Abstract

The brain vasculature can be investigated in different ways ranging from in vivo to biochemical analysis. Immunohistochemistry is a simple and powerful technique that can also be applied to archival tissues. However, staining of brain vessels on paraffin sections has been challenging. In this study, we developed an optimized method that can be used in paraffin-embedded mouse and human brain tissues derived from healthy controls and neurological disorders such as Alzheimer's disease. We subsequently showed that this method is fully compatible with the detection of glial cells and key markers of Alzheimer's disease including amyloid beta and phosphorylated Tau protein. Furthermore, we observed that the length of microvasculature in hippocampus of TgCRND8 Alzheimer's disease mouse model is reduced, which is correlated with the decreased blood flow in hippocampus as determined by arterial spin labeling perfusion magnetic resonance imaging. Finally, we determined that the microvasculature length in two other Alzheimer's disease mouse models, APP and PS1 double-transgenic mice and P301S Tau-transgenic mice, is also shortened in the dentate gyrus. Thus, we have established a new, simple and robust method to characterize the brain vasculature in the mouse and human brain.

Keywords Blood vessels · Antigen retrieval · Immunohistochemistry · Cerebral blood flow · Alzheimer's disease

Introduction

The role of cerebrovascular dysfunction is becoming widely recognized in dementia and Alzheimer's disease (AD) (Love and Miners 2016; Montagne et al. 2016). Cerebrovascular diseases (CVD) and AD share multiple risks factors including hypertension, diabetes mellitus, hypercholesterolemia, APOE ε4 and age (Love and Miners 2016). AD and CVD are both alone sufficient to lead to dementia, nevertheless the effects of their combination are controversial (Attems and Jellinger 2014).

One of the main features of CVD is the reduction of cerebrovascular blood flow. Hypoperfusion is an early pathophysiological feature in AD patients as well and appears before cognitive decline and amyloid β deposition (Asllani et al. 2008; Binnewijzend et al. 2013). In APP-transgenic AD mouse models, the permanent ligation of the common carotid artery causes chronic cerebral hypoperfusion, which has been shown to accelerate the cognitive decline in association with increased Aβ deposition in the brain parenchyma (Bordeleau et al. 2016).

Yang Liu and Klaus Fassbender share the senior authorship.

Electronic supplementary material The online version of this article (https://doi.org/10.1007/s00429-017-1595-8) contains supplementary material, which is available to authorized users.

✉ Yann Decker
Yann.Decker@uks.eu

1 Department of Neurology, University of the Saarland, Kirrberger Strasse, 66421 Homburg/Saar, Germany

2 German Institute for Dementia Prevention (DIDP), University of the Saarland, 66421 Homburg/Saar, Germany

3 Clinic of Diagnostic and Interventional Radiology, Saarland University Medical Center, 66421 Homburg/Saar, Germany

4 Department of Neuropathology, University of the Saarland, 66421 Homburg/Saar, Germany

5 Department of Neurology, Universitätsmedizin Mannheim, Heidelberg University, Mannheim, Germany

6 Institute for Clinical and Experimental Surgery, Saarland University, 66421 Homburg/Saar, Germany

While hypoperfusion is a well-established hallmark of AD in patients and in its various animal models (Faure et al. 2011; Hebert et al. 2013; Massaad et al. 2010; Poisnel et al. 2012), its cause and role in the pathogenesis of AD is still not fully understood. In AD patients, a decrease in microvascular density has been observed and proposed as one of the reasons of hypoperfusion (Bouras et al. 2006; Buee et al. 1994; Love and Miners 2016). Studies focusing on histological analysis have also described alterations of the microvasculature in different mouse models of AD (Kouznetsova et al. 2006; Lee et al. 2005; Zerbi et al. 2013). However, none of these studies have directly correlated microvasculature damage to a reduction of cerebral blood flow.

Thus, we decided to evaluate both microvasculature density and cerebral blood flow in a well-characterized APP-transgenic AD mouse model, which is known to carry impaired cerebral microvasculature (Dorr et al. 2012; Paul et al. 2007). Unfortunately, the staining of the microvasculature by immunohistochemistry on paraformaldehyde-fixed adult rodent brains has been recognized to be inconsistent and the reasons are not entirely understood (Jucker et al. 1992; Mori et al. 1992).

To overcome the inconsistencies of standard immunohistochemistry, we have developed a new method to detect the blood vasculature on paraffin sections of adult mouse and human brains. We further compared the length of hippocampal blood vessels visualized on 40-µm-thick paraffin sections with the cerebral blood flow measured by arterial spin labeling analysis in both APP-transgenic and wild-type mice.

Materials and methods

Animals

TgCRND8 APP-transgenic mice (APP) expressing a transgene that incorporates both the Indiana mutation (V717F) and the Swedish mutations (K670N/M671L) in the human app gene under the control of hamster prion protein (PrP) promoter (Chishti et al. 2001) were kindly provided by D. Westaway (University of Toronto, Canada). Number of animals used for MRI: APP $n=6$, WT littermates $n=7$, histological studies: APP $n=8$ and WT littermates $n=11$.

APP/PS1 double transgenic mice overexpressing human-mutated APP (KM670/671NL) and PS1 (L166P) under Thy-1 promoters (Radde et al. 2006) were kindly provided by M. Jucker (University of Tübingen, Germany).

Number of animals used: APP/PS1 $n=8$, WT littermates $n=7$.

P301S Tau-transgenic mice (B6;C3-Tg(Prnp-MAPT*P301S) PS19Vle/J; stock no. 008169) overexpressing the mutant human Tau (P301S) gene under the direction of the mouse prion protein promoter (Yoshiyama et al. 2007) were purchased from The Jackson Laboratory (Maine, USA). Number of animals used: P301S $n=6$, WT littermates $n=6$.

NG2-CreERT2 mice ($n=2$) that were crossbred with the reporter mouse line Rosa26-CAG-floxed-stop-tdTomato (Huang et al. 2014) were kindly provided by F. Kirchhoff.

Mice were housed at a 12 h day/12 h night cycle with free access to tap water and food pellets. All animal experiments were approved by the regional ethical committee of the Saarland, Germany.

Humans

Paraffin-embedded brain samples from AD patients were obtained from the Department of Neuropathology of Saarland University. The use of post-mortem human brains was approved by the local ethical committee. The clinical diagnosis of AD was confirmed by histochemical staining of senile plaques and neurofibrillary tangles.

Tissue collection for pathological analysis

Animals were euthanized at the indicated age by inhalation of isoflurane (Abbott, Wiesbaden, Germany). Mice were then perfused transcardially with ice-cold PBS, the brain was removed and divided. The left hemisphere was immediately fixed in 4% PFA (Sigma, Schnelldorf, Germany) and embedded in paraffin for histological analysis.

Antigen retrieval

Antigen retrieval was performed after rehydration of 40-µm paraffin sections as following. For heat antigen retrieval, sections were heated with a steamer at 80 °C in citrate buffer (10 mM, pH = 6) for 1 h. Sections were allowed to cool down at room temperature. Before enzymatic antigen retrieval, sections were washed twice with distilled water and next treated with digest-all™ 3 Pepsin (Life Technologies, Karlsruhe, Germany) without dilution at 37 °C for 20 min.

Immunohistochemistry and lectin staining

Following antigen retrieval, 40-µm-thick sagittal paraffin sections were incubated with the primary rabbit antibody against collagen IV at 4 °C overnight (1:500; # ab6586, Abcam Cambridge, UK). After three washes with PBS, the VectaStain Elite ABC-AP kit (Vector Laboratories, Burlingame, CA, USA) and the Vector Blue Alkaline Phosphatase Substrate kit (Vector Laboratories) were used according to the manufacturer's instructions. Sections were counterstained with fast red (Sigma). After dehydration steps, coverslips were mounted with Vecta mount™ (Vector Laboratories).

Fluorescent staining was performed on 40-µm paraffin sections after the indicated antigen retrieval procedure.

The primary rabbit antibodies were anti-collagen IV (1:500; Abcam, # ab6586), anti-laminin (1:300; Abcam, #11575), anti-Iba1 (1:500; #019-19741, Wako Chemicals GmbH, Neuss, Germany) and anti-red fluorescent proteins (1:100, #600-401-379, Biomol, Plymouth Meeting, PA, USA). The primary mouse antibodies were anti-$A\beta_{42}$ (1:500, MOAB-2, clone 6C3; Biomol), anti-p-Tau (1:500, clone AT8; Thermo Scientific, Darmstadt, Germany), anti α-SMA (1:500, clone 1A4; Sigma) and anti GFAP (1:500, clone 2A5; Abcam, # ab4648). All primary antibodies were incubated at 4 °C overnight. After washing sections, they were incubated with Alexa Fluor 488-conjugated goat anti-rabbit IgG or goat anti-mouse IgG (1:250, Life Technologies). For lectin staining, sections were incubated with DyLight® 488-labeled tomato lectin (1:100, DL-1174, Vector Laboratories) at 4 °C overnight. For double staining, incubations with the primary and secondary antibodies were performed successively (secondary antibodies were applied for 2 h at room temperature). Coverslips were mounted with Mowiol® (Sigma) including DAPI (Sigma).

Image acquisition and analysis

All images were acquired with a Zeiss AxioImager Z2 microscope equipped with a stereo investigator system (MicroBrightField, Williston, VT, USA). Using the virtual tissue scan module of stereo investigator, we performed multichannel acquisitions of the regions of interest on the sections.

Blood vessel length quantification

The virtual section was specifically cropped to delimitate the region of interest. As shown in supplementary Fig. 1, vessels were next thresholded, despeckled and skeletonized with the ImageJ plugin "Skeletonize3D" as previously described (Whiteus et al. 2014).The length of skeletonized vessels was automatically quantified with the ImageJ plugin "AnalyzeSkeleton". The total length of vessels measured was summed and divided by the area of the region of interest. To ensure accurate counts, every tenth 40-µm sections throughout the brain (in total four sections per brain) were selected, stained and analyzed. For α-SMA positive vessel quantification, in case of round vessels, they were filled manually with ImageJ after the threshold step.

Blood vessel diameter quantification

The virtual section was specifically cropped to delimitate the region of interest. To measure vessel diameter, the pictures were thresholded. Minimum Feret's diameter was determined with ImageJ software and was used as an approximation for vessel diameter as previously described (Kloepper et al. 2016).

To ensure accurate counts, every tenth 40-µm sections throughout the brain (in total four sections per brain) were selected, stained and analyzed.

MRI measurements of cerebral blood flow

Seven APP-wild-type and six APP-transgenic mice were examined at the age of 8 months with a horizontal bore 9.4 T MRI animal scanner (Bruker BioSpin 94/20, Ettlingen, Germany) using a high-performance water-cooled gradient system with a gradient strength of 675 mT/m, a linear inductive rise time of 130 µs and a maximum slew rate of 4673 T/m/s. The magnetic resonance imaging (MRI) system was run with the ParaVision 6.0.1, including the arterial spin labeling (ASL) MRI protocol employed for determination of global and regional cerebral blood flow (CBF). An actively decoupled four element (2 × 2) surface coil designed for the mouse brain (Bruker BioSpin) was used for signal acquisition, while a single-channel volume coil with an inner diameter of 72 mm was used for RF pulse transmission (Bruker BioSpin).

All experiments were performed with animals under general anesthesia with a mixture of 1.0–2.0% isoflurane and 99–98% oxygen at a flow rate of 1.5 L/min. Induction and maintenance as well as animal monitoring and handling during MRI experiments were performed as described previously (Fries et al. 2012). Animal core temperature was controlled by manual adjustment of the animal heating device and maintained at 36.5–38.5 °C throughout MRI data acquisitions. Standard MRI settings are summarized in Table 1.

Animal position was verified within the magnet with a fast low angle shot (FLASH) localizer MRI sequence

Table 1 Detailed parameters of the applied sequences as set in paravision 6.0.1

Sequence	TR (ms)	TE (ms)	Flip angle	ST (mm)	FOV (mm^2)	Matrix	NS	NA	Duration
Flash	15.0	3.0	10°	1.0	25.0 × 25.0	192 × 192	3 × 5	3	2 m 9 s 600 ms
Rare	1300.0	32.0	90°/180°	0.8	20.0 × 12.8	268 × 170	11	8	3 m 38 s 400 ms
Fair-EPI	10000.0	16.5	90°/180°	0.8	20.0 × 12.8	100 × 65	1	4	17 m 33 s 770 ms

TR repetition time, *TE* echo time, *ST* slice thickness, *FOV* field of view, *NS* number of slices, *NA* number of averages

generating image sets in *x, y* and *z* orientations. Preceding anatomical MRI and CBF measurements extensive iterative first- and second-order shimming was performed with a special protocol supplied with the scanner software, followed by readjustment of basic resonance frequency and reference pulse strength.

For identification of different portions of the hippocampus, a standard T2-weighted rapid acquisition relaxation-enhanced (RARE) MRI scan of the whole brain was obtained with 11 axial slices spanning from the trailing edge of the olfactory bulb to the leading edge of the cerebellum. Anatomical T2-weighted images were acquired with prospective respiratory triggering, motion averaging, fat suppression, flip back pulse and a RARE factor of eight.

For each animal investigated, a single slice of interest was determined as the second axial section from rostral in which the hippocampus could be identified (Fig. 5a, b). For CBF measurements, the geometry of these single slices was loaded into an echo planar imaging (EPI)-based flow sensitive alternating inversion recovery (FAIR) MRI sequence (Kim et al. 1997). FAIR EPI MRI was performed in interleaved mode with constant recovery time, fat suppression and 12 selective and non-selective experiments each. Inversion times TI were set to 30, 100, 300, 600, 900, 1000, 1050, 1100, 1150, 1300, 1600 and 2400 ms. Inversion slab thickness and slice package margin were set to 3.8 and 1.5 mm, respectively.

T1 values from the scans with selective and non-selective inversion pulses were calculated using the t1invacq function of Paravision 6.0.1 on a voxel-by-voxel basis, creating T1 maps from both experiments. From selective and non-selective inversion T1 maps, CBF maps were calculated with the Paravision 6.0.1 macro ASL_Perfusion_Processing employing equations published previously (Herscovitch and Raichle 1985; Kober et al. 2007), with the T1 of blood set to 2400 ms (Dobre et al. 2007), encoded in grey scale as well as in false color (Fig. 5c–f). Regions of interest (ROI) circumscribing both hippocampi and the brain were transferred from the corresponding anatomical images to the CBF maps. Individual voxels selected for measurements were verified to reside in desired anatomical structures, ROI were adjusted when necessary and average values for CBF (in mL min^{-1} 100 g $tissue^{-1}$) were collected.

Statistics

Two-independent-sample *t* test was used to compare means for two groups. Pearson correlation and *t* test statistical analyses were performed with SPSS version 19.0 for Windows (IBM, New York, NY, USA). Statistical significance was set at the level of $p < 0.05$. All box plots were plotted using BoxPlotR (Spitzer et al. 2014).

Results

The sequential treatment with citrate and pepsin is an efficient method to recover antigens on paraffin-embedded brain tissues

To visualize the blood vasculature of adult mouse brain, different antigen recovery methods were tested for the immunohistochemical staining of collagen IV on 40-µm-thick paraffin sections. No antigen retrieval led to ineffective immunostaining (Fig. 1a). Heating the sections for 1 h at 80 °C in citrate buffer at pH = 6 was not effective either at unmasking antigens for collagen IV (Fig. 1b). Increasing the treatment duration up to 2 h or the temperature up to 100 °C did not lead to further improvements (data not shown). Therefore, a pepsin treatment similar to the one described on paraformaldehyde-fixed free-floating sections (Franciosi et al. 2007) was applied to paraffin-embedded tissues. Unexpectedly, the pepsin treatment did not allow collagen IV visualization (Fig. 1c). We then combined citrate buffer treatment followed by pepsin treatment and observed a remarkable increase in collagen IV immunoreactivity (Fig. 1d). Heating sections in a steamer or a microwave (data not shown) led to comparable intensities of immunostainings; however, steam treatment limited tissue damage. Additional replacement of citrate buffer by distilled water gave similar results suggesting that heat is critical in this process (data not shown). Surprisingly, when digestion with pepsin was applied before heat treatment, no staining with anti-collagen IV antibody was observed (Fig. 1e). The intensity and homogeneity of the immunostaining after sequential treatment with citrate and pepsin combined with stereological microscopy allowed the reconstitution of a sagittal section of the cortex and hippocampus of an adult mouse brain (Fig. 1f).

When testing the optimized protocol on 40-µm-thick paraffin sections cut from human brains, we have observed that similarly to adult mouse tissues, a combination of heat followed by enzymatic digestion was necessary to obtain the optimal staining of the vasculature in the cortex (Fig. 2a–e).

To further investigate the role of pepsin treatment, brain sections were subjected to different time periods of enzymatic digestion (Fig. 2f–j). Slides treated with pepsin for 2–10 min following heat antigen retrieval with citrate buffer for 1 h, showed partial detection of the brain vasculature (Fig. 2f–h). Digestion of the brain tissue for 20 min appeared to be optimal, revealing a maximal intensity and complexity of the vasculature (Fig. 2i). Increasing time of treatment with pepsin did not increase immunoreactivity but led to increased tissue damage (data not shown). When the optimal time of pepsin digestion (i.e. 20 min) preceded heat treatment, no collagen IV immunoreactivity was visible (Fig. 2j).

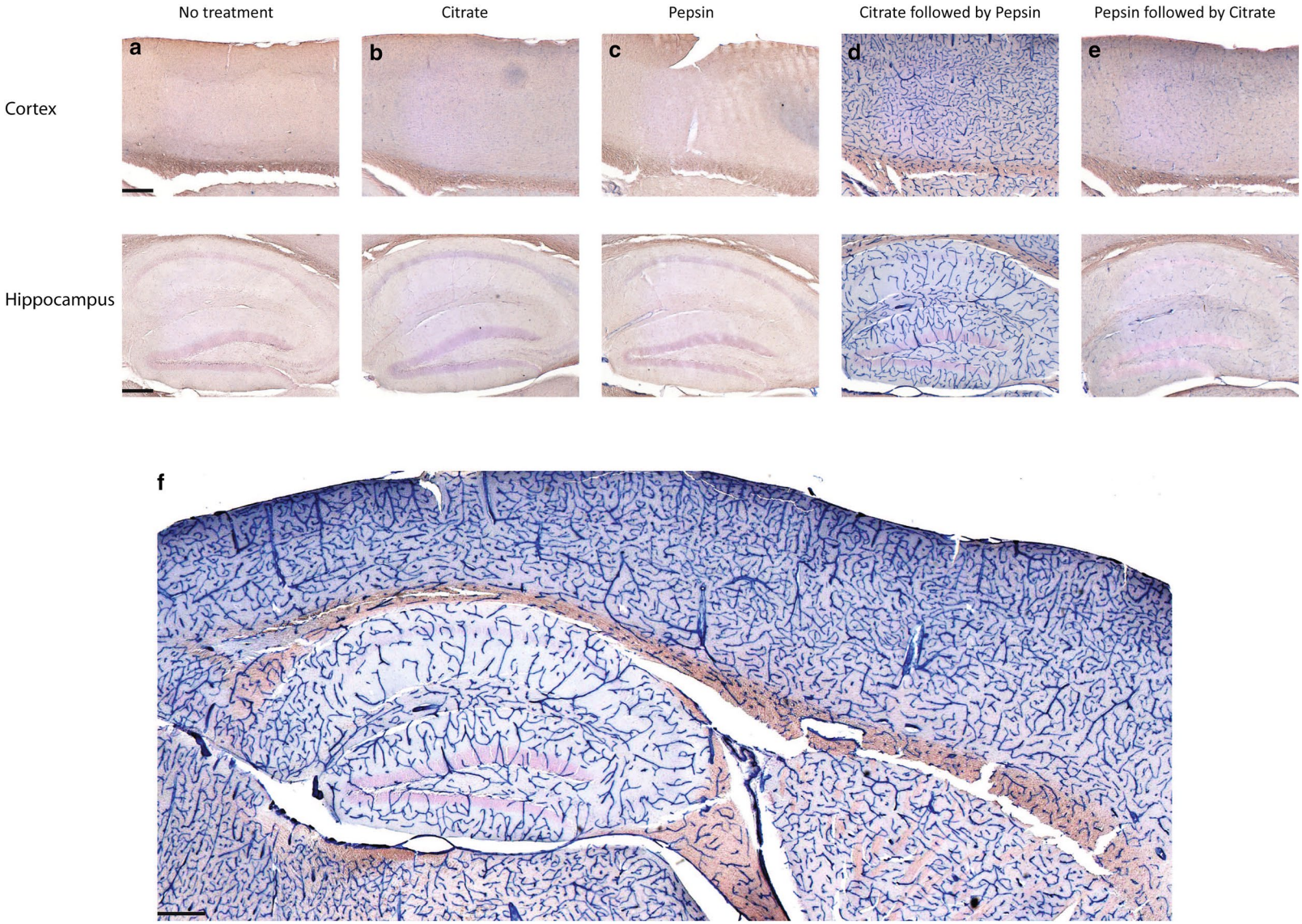

Fig. 1 Citrate–pepsin-combined antigen retrieval treatment enhances collagen IV immunostaining. Representative images of 8-month-old mouse paraffin sections (40 µm) showing cortex (upper panels) and hippocampus (lower panels) stained with collagen IV antibody (**a**–**e**). Staining following no antigen retrieval pretreatment (**a**), antigen retrieval with citrate alone (**b**), pepsin alone (**c**), a combination of citrate preceding pepsin (**d**) and pepsin preceding citrate (**e**). **f** Representative virtual tissue reconstitution of collagen IV staining following the combination of citrate preceding pepsin treatment. Scale bar 250 µm

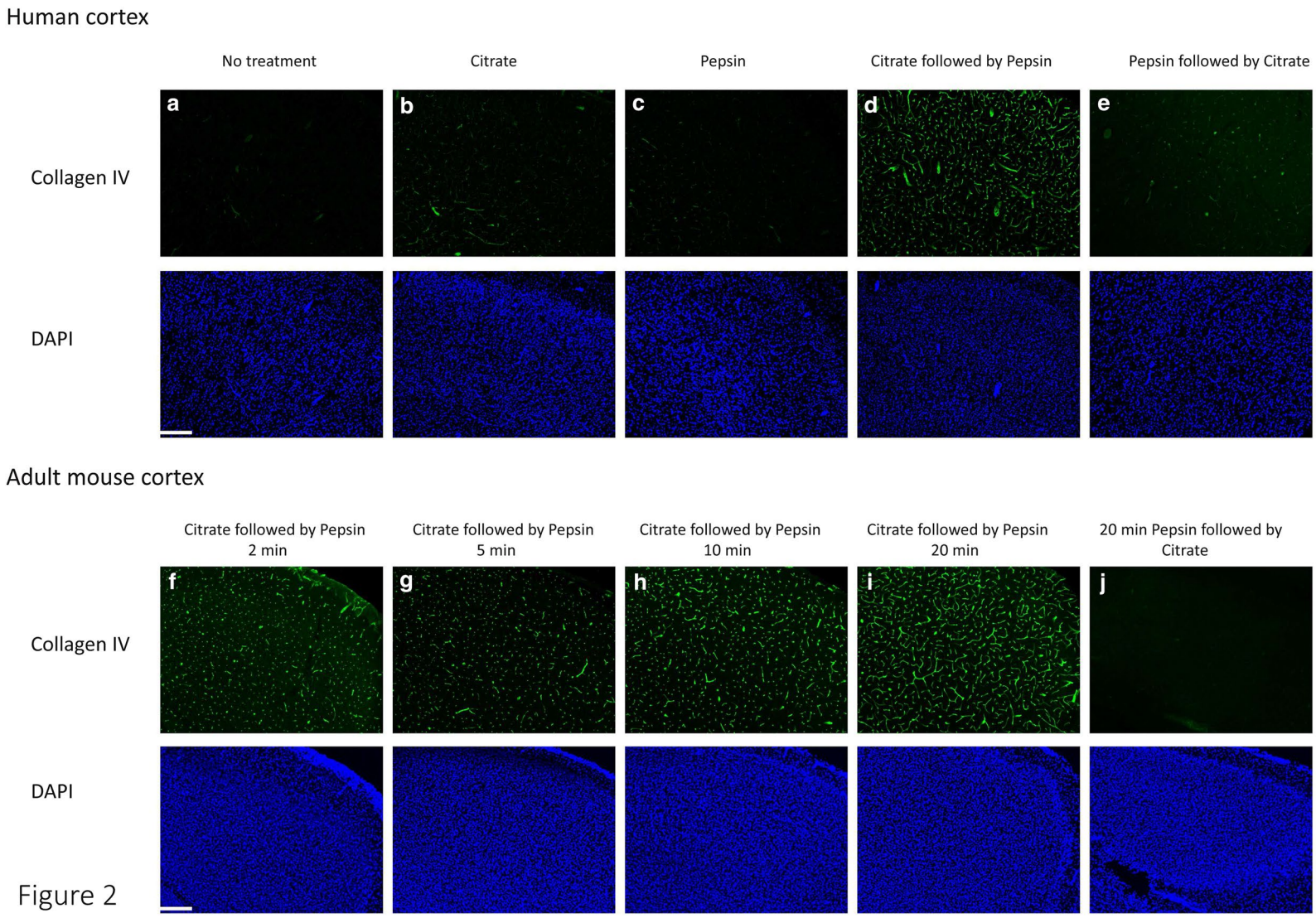

Fig. 2 Citrate–pepsin-combined antigen retrieval enhances collagen IV staining on paraffin-embedded human brain sections; collagen IV immunoreactivity directly depends on the time of treatment with pepsin. Effect of different antigen retrieval treatments on 40-µm serial paraffin sections of the cortex of an Alzheimer's disease patient. Staining of collagen IV (green, upper panels) and counterstaining with DAPI (blue, lower panels) following no antigen retrieval pretreatment (**a**), antigen retrieval with citrate alone (**b**), pepsin alone (**c**), combination of citrate preceding pepsin (**d**) and pepsin preceding citrate (**e**). Following a first heat-mediated antigen retrieval treatment with citrate buffer, mouse brain slides were subjected to different times (2–20 min) of incubation with pepsin (**f–i**). In (**j**) the section was first treated with pepsin before citrate treatment. The tissues were next stained with collagen IV antibody (green, upper panels) and counterstained with DAPI (blue, lower panels) (**f–j**). Scale bar 250 µm

Using the optimal protocol, we further examined alternative classical markers of blood vessels: tomato lectin and laminin. Vessel staining in adult mouse brain with tomato lectin (Fig. 3a–e) and laminin (Fig. 3f–j) revealed to be as robust as the anti-collagen IV staining only when heat preceded enzymatic treatment. Altogether, these findings support the view that the combined antigen retrieval method we propose can be broadly applied for a diversity of brain antigens.

The citrate and pepsin-based antigen retrieval protocol is compatible with the staining of vasculature and other AD-related typical markers

After we optimized the antigen retrieval protocol for the immunohistological staining of vasculature, we asked whether this protocol was compatible for the staining of other AD-related proteins. We tested this protocol in the co-labeling of blood vessels and amyloid-β (Aβ), p-Tau or Iba1. Both Aβ (Fig. 4a–f) and p-Tau (Fig. 4g–h) showed enhanced antigenic reactivity following serial treatments with citrate and pepsin compared to the standard antigen retrieval protocol with single citrate buffer treatment (data not shown). Cerebral amyloid angiopathy and Aβ plaque interactions with blood vessels were observed both in mouse (Fig. 4c, e) and human (Fig. 4d, f) brain sections embedded in paraffin. Detection of microglial cells with Iba1 antibody was also possible (Fig. 4i–j), albeit the signal was not increased when compared to our routine staining protocol (data not shown). We could also show that the co-detection of astrocytes and blood vessels was possible (supplementary Figs. 2a, b). Although we failed at directly staining pericytes following heat and enzymatic treatment (data not shown), we were able to successfully detect immunologically the red fluorescent protein in NG2-CreERT2 mice that were crossbred with Rosa26-tdTomato animals (supplementary Figs. 2c, d).

The total length of vasculature is correlated with the cerebral blood flow in the hippocampus

After establishing the method for immunohistological staining of cerebral vasculature, we continued to investigate whether this protocol could be used to evaluate cerebrovascular dysfunction in the AD brain. Thus, we measured cerebral blood flow in APP-transgenic and wild-type mice with MRI and compared it with the anatomical changes in the vasculature of the same mice. In MRI experiments, regions of interest, i.e. brain and hippocampus for cerebral blood flow analysis, were identified in T2-weighted anatomical images (Fig. 5a, b). Utilizing ASL MRI, the blood flow was measured in the brain and the hippocampus of 8-month-old TgCRND8 APP-transgenic and wild-type littermate mice (Fig. 5c–f). While in the whole brain of APP mice, the blood flow (Fig. 5g) was reduced by 6% ($p = 0.055$) when compared to wild-type animals, the regional CBF in the cortex and in the hippocampi were respectively 9% ($p = 0.055$) and 20% ($p < 0.001$) lower in transgenic mice than in the littermate controls (Fig. 5h–i). Thus, we restricted the comparison of the blood flow and the length of blood vessels to the hippocampus. A significant correlation was observed between the hippocampal blood vessel length and the hippocampal blood flow (Fig. 6a), (Pearson correlation $R = 0.754$; $p = 0.003$) but not between the cortical blood vessel length and the cortical blood flow (Fig. 6b), (Pearson correlation $R = 0.754$; $p = 0.003$).

To determine which vascular compartment might be affected, we measured the diameter of capillaries (< 6 µm in diameter) and larger vessels (> 6 µm in diameter) in the hippocampus of TgCRND8 APP-transgenic mice and their wild-type littermates (Fig. 6c, d). We observed a significant reduction ($p < 0.05$) of the capillary diameter in the AD mouse model (Fig. 6c). We further investigated whether the vascular morphological changes could originate from α smooth muscle actin-positive (α-SMA) vessels. We stained (Fig. 6e) and quantified the length of α-SMA-positive vessels (Fig. 6f) in the hippocampus of TgCRND8 and WT mice. No difference was observed between APP mice and the control.

In the following experiments, we used the optimized method to evaluate the brain microvasculature in three different and complementary mouse models of AD. Because these three models share the strongest expression of Aβ (Fig. 7a, b) or p-Tau in the dentate gyrus (Fig. 7c), we focused our evaluation of the brain vasculature in this area. Remarkably, we observed structural alterations of the microvasculature at the age of 8 months in all three models. In comparison with their age-matched wild-type controls, the blood vessel length was shorter in TgCRND8 APP mice (Fig. 7d) by 11% ($p < 0.01$), in APP and PS1 double transgenic mice (Fig. 7e) by 7% ($p < 0.01$) and in P301S Tau-transgenic mice (Fig. 7f) by 9% ($p < 0.05$).

Discussion

Detection and quantification of the brain vasculature is easily performed in neo-natal rodents (Walchli et al. 2015), however poor or inconsistent staining has been observed in paraformaldehyde-fixed adult brains (Jucker et al. 1992; Mori et al. 1992). Recently, pepsin digestion has been described to enable a widespread staining of the vessel basement membrane in the adult mouse brain (Franciosi et al. 2007). Requirement of pepsin to visualize brain blood vessels has been confirmed both on frozen (Clark et al. 2009; Muneton-Gomez et al. 2012; Soto et al. 2015) and vibratome sections (Gama Sosa et al. 2014; Gama Sosa et al. 2010). However,

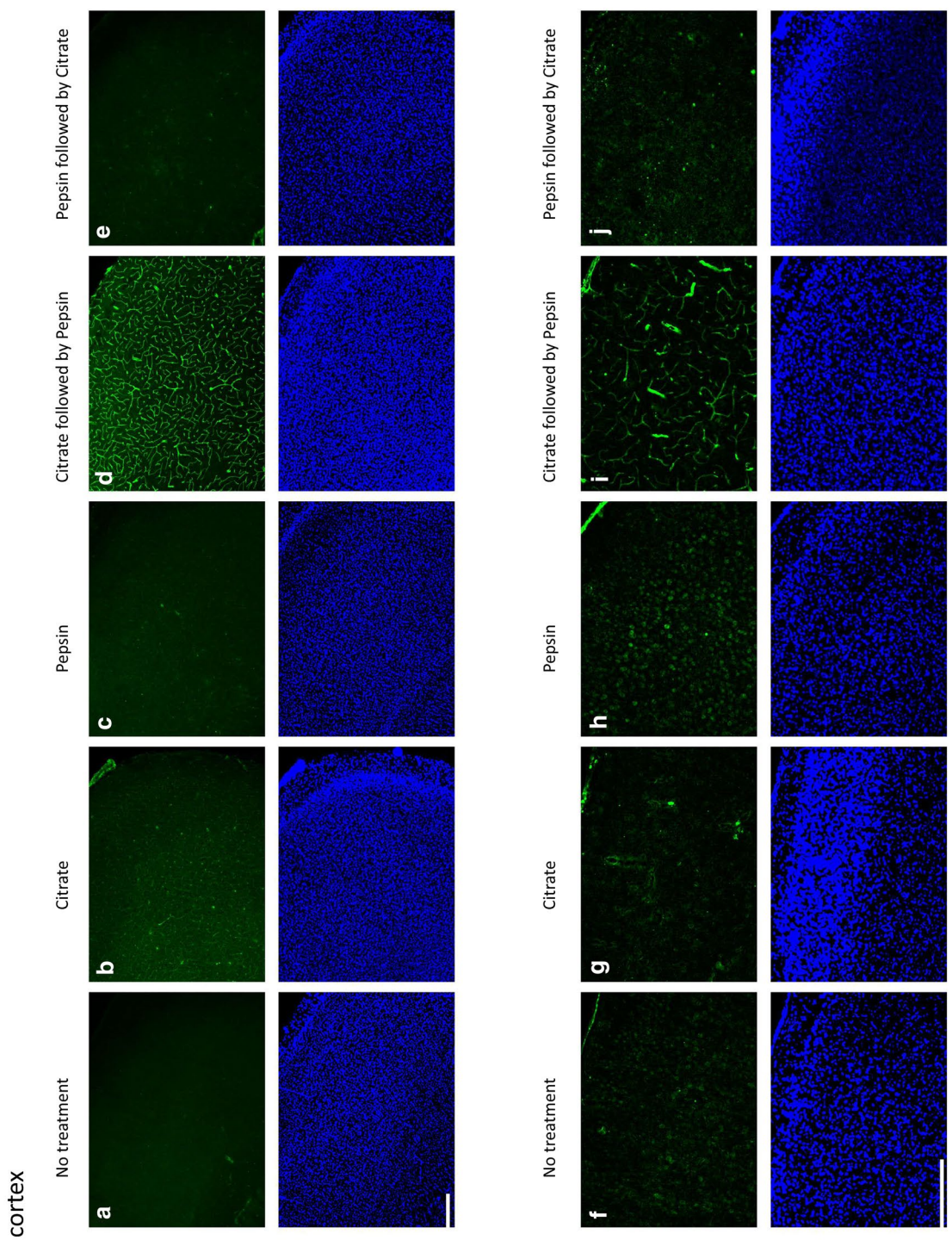

Fig. 3 Citrate–pepsin-mediated antigen retrieval treatment enhances the cerebral staining of multiple blood vessel antigens in the adult mouse brain. Example of images showing cerebral vascular staining (green, upper panels) with tomato lectin (**a–e**) or laminin (**f–j**) and counterstained with DAPI (blue, lower panels). Staining was performed on 40-µm-thick paraffin sections of 8–month-old mice. No antigen retrieval (**a, f**), antigen retrieval with citrate alone (**b, g**), pepsin alone (**c, h**) and combination of pepsin preceding citrate (**e, j**) did not lead to robust staining of the brain vasculature. The unique combination of citrate preceding pepsin antigen retrieval led to strong and homogenous staining of brain blood vessels (**d, i**). Scale bar 250 µm

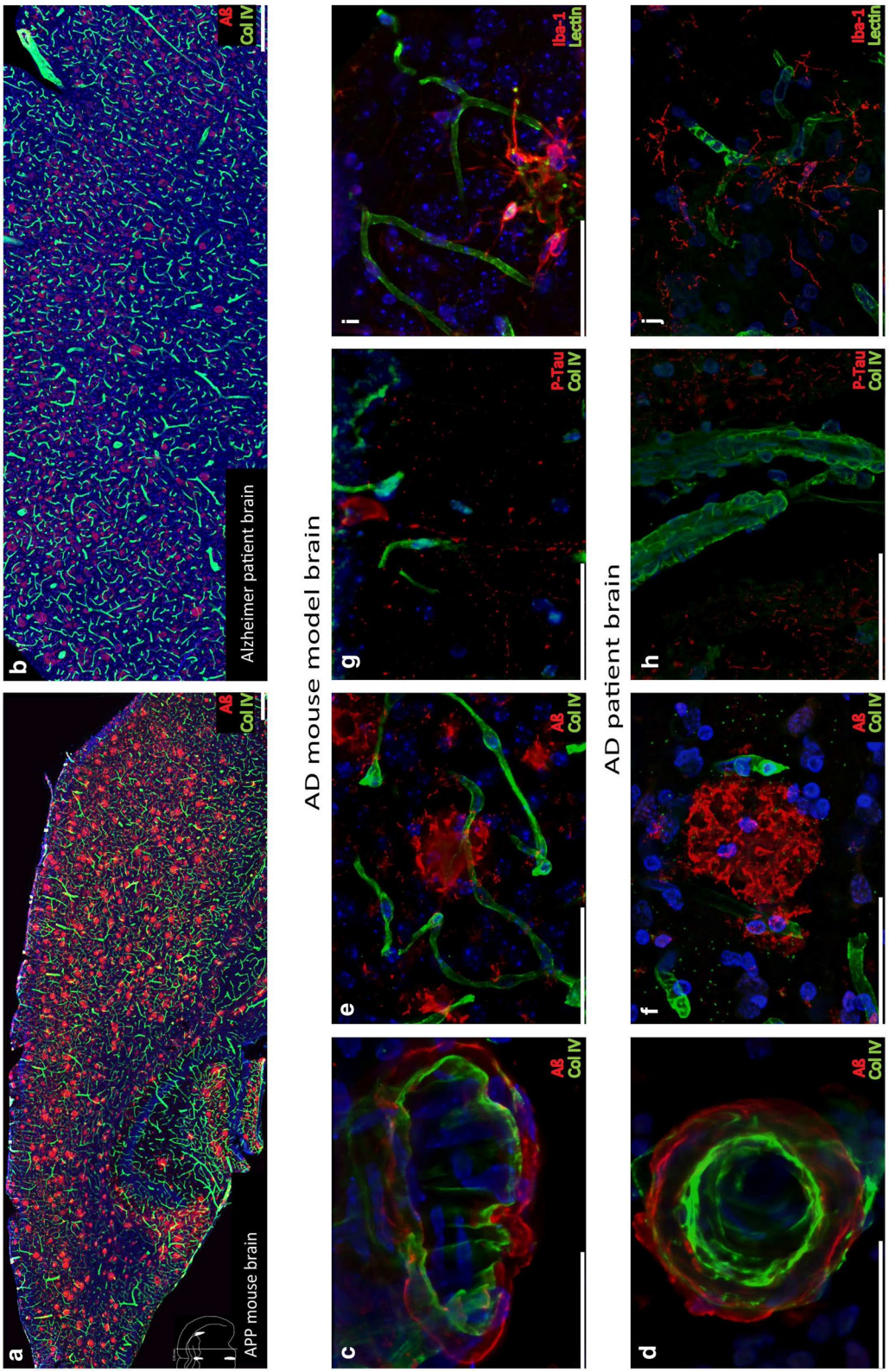

Fig. 4 Citrate–pepsin-combined antigen retrieval method does not interfere with key markers of Alzheimer's disease either in mouse or in human brains. Virtual tissue reconstruction of collagen IV and amyloid β peptide immunofluorescence staining following the combined antigen retrieval treatment (citrate followed by pepsin) in adult TgCRND8 mouse (**a**) and in a patient diagnosed with Alzheimer's disease (**b**). Scale bar 250 µm. Illustration of co-staining with collagen IV and amyloid β and p-Tau in AD mouse models (**c, e, g**) or in AD brain tissues (**d, f, h**). For co-staining with Iba-1, tomato lectin was used in mouse (**i**) and in human (**j**) brain sections. Scale bar 50 µm

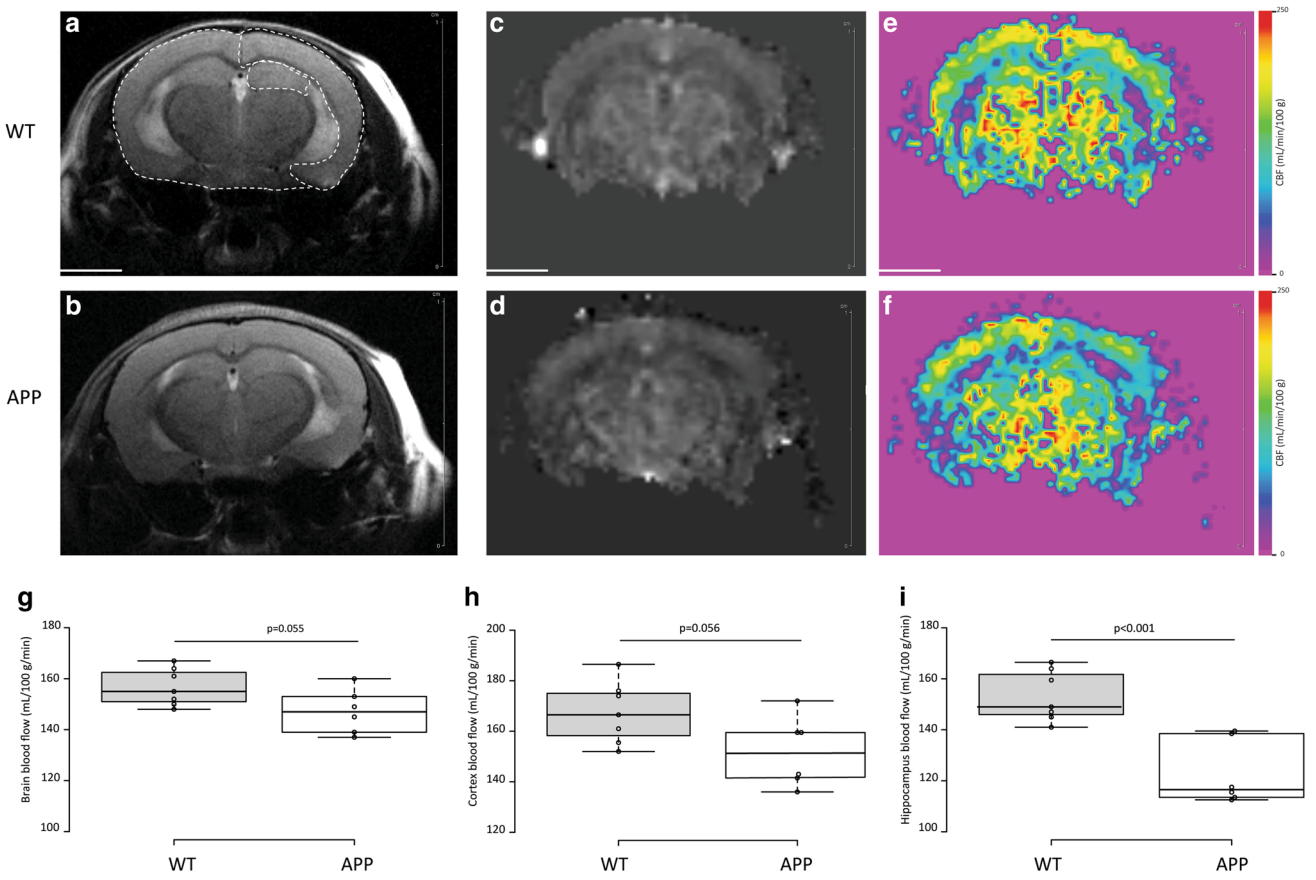

Fig. 5 Cerebral blood flow (CBF) is reduced in the hippocampus of TgCRND8 (APP) mice. T2-weighted anatomical images of WT (**a**) and APP (**b**) mouse brains showing regions of interest (brain, cortex and hippocampus) selected for cerebral blood flow (CBF) measurements. Absolute grey scale CBF maps and false color CBF maps obtained with arterial spin labeling magnetic resonance perfusion imaging at 9.4T in 8-month-old WT (**c, e**) and APP (**d, f**) mice. Quantification and comparison in WT and APP mice of the brain ($p=0.055$), cortical ($p=0.056$) and hippocampal ($p<0.001$) blood flow (**g–i**). Horizontal lines in the box represent medians, box limits indicate the 25th and 75th percentiles, whiskers extend 1.5 times the interquartile range from the 25th and 75th percentiles and individual animals are represented as open circles. Bars indicate 1 cm. *p* values by unpaired *t* tests are indicated in the plots for (**g–i**). Scale bar 250 µm

we and others (Vollert et al. 2015) had failed at visualizing blood vessels on paraffin sections in spite of pepsin treatment. Our newly established protocol combining heat and enzymatic treatment has allowed us to stain the brain vasculature on paraffin sections.

Paraffin sections offer many advantages over vibratome or frozen sections including a better preservation of the tissue structure and the possibility to access to a larger resource of archival tissues. Heat treatment is the major antigen retrieval method used in routine immunohistochemistry (Shi et al. 1991). An alternative is to use enzymatic digestion to restore the immunoreactivity of antigens on paraffin sections (Huang et al. 1976). Publications reporting heat or enzymatic treatment are largely abundant, however, the combination of heat and enzymatic treatment is rarely described in the literature (D'Amico et al. 2009). The mechanism of heat-induced antigen retrieval is based on the cleavage of protein–protein crosslinks (Yamashita 2007). Concerning pepsin treatment, Mauro et al. suggested that it might disrupt cross links between laminin and collagen (Mauro et al. 1984). Remarkably, in the antigen retrieval method we propose only a pretreatment of paraffin-embedded sections with heat followed by enzymatic treatment leads to a robust staining of blood vessels. Enzymatic treatment preceding heating was ineffective. A possible mechanism could be that heat treatment is necessary to remove the trace amount of paraffin remaining in the tissue and/or to break protein crosslinks to enable further penetration and action of pepsin.

Alzheimer's disease is a disorder characterized by abnormal aggregation of Aβ, hyperphosphorylation of Tau and activation of glial cells (De Strooper and Karran 2016). Aβ, p-Tau and glial cells interact with the brain vasculature (Dudvarski Stankovic et al. 2016; Lamoke et al. 2015; Love and Miners 2016). Interestingly, our antigen retrieval

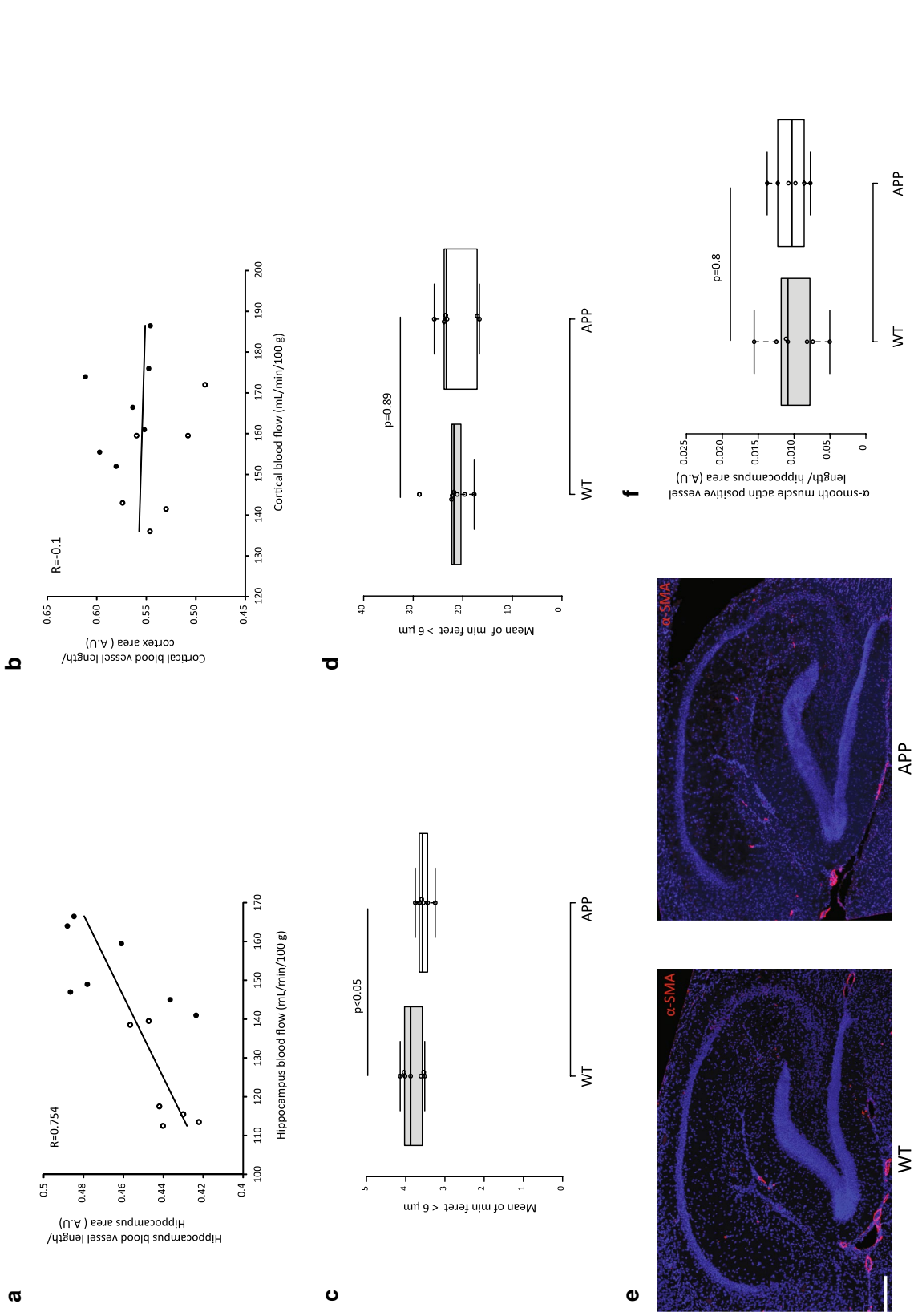

Fig. 6 Cerebral blood flow (CBF) correlates with blood vessel length in the hippocampus; capillary diameter is reduced in the hippocampus of TgCRND8 mice. Relationship between capillary length/area determined after immunostaining followed by automatized quantification and microvasculature blood flow measured by arterial spin labeling in the hippocampus (**a**) and the cortex (**b**) of wild-type (filled circles) and APP (open circle) mice. The lines depict the linear regression, Pearson correlation coefficient in the hippocampus (**a**) $R = 0.754$, $p = 0.003$ and in the cortex (**b**) $R = -0.1$, $p = 0.692$. Minimum Feret's diameter was used as an approximation for vessel diameter. The means of the vessels whose diameter was < 6 µm (**c**) and > 6 µm (**d**) were calculated in the hippocampus of TgCRND8 and control mice. Representative pictures of α-smooth muscle actin (α-SMA) vessels in the hippocampus of TgCRND8 mice and their wild-type littermates (**e**). Automated quantification of α-SMA positive vessels in the hippocampus of transgenic and wild-type control mice indicates no change in the vessel length ($p = 0.8$) (**f**)

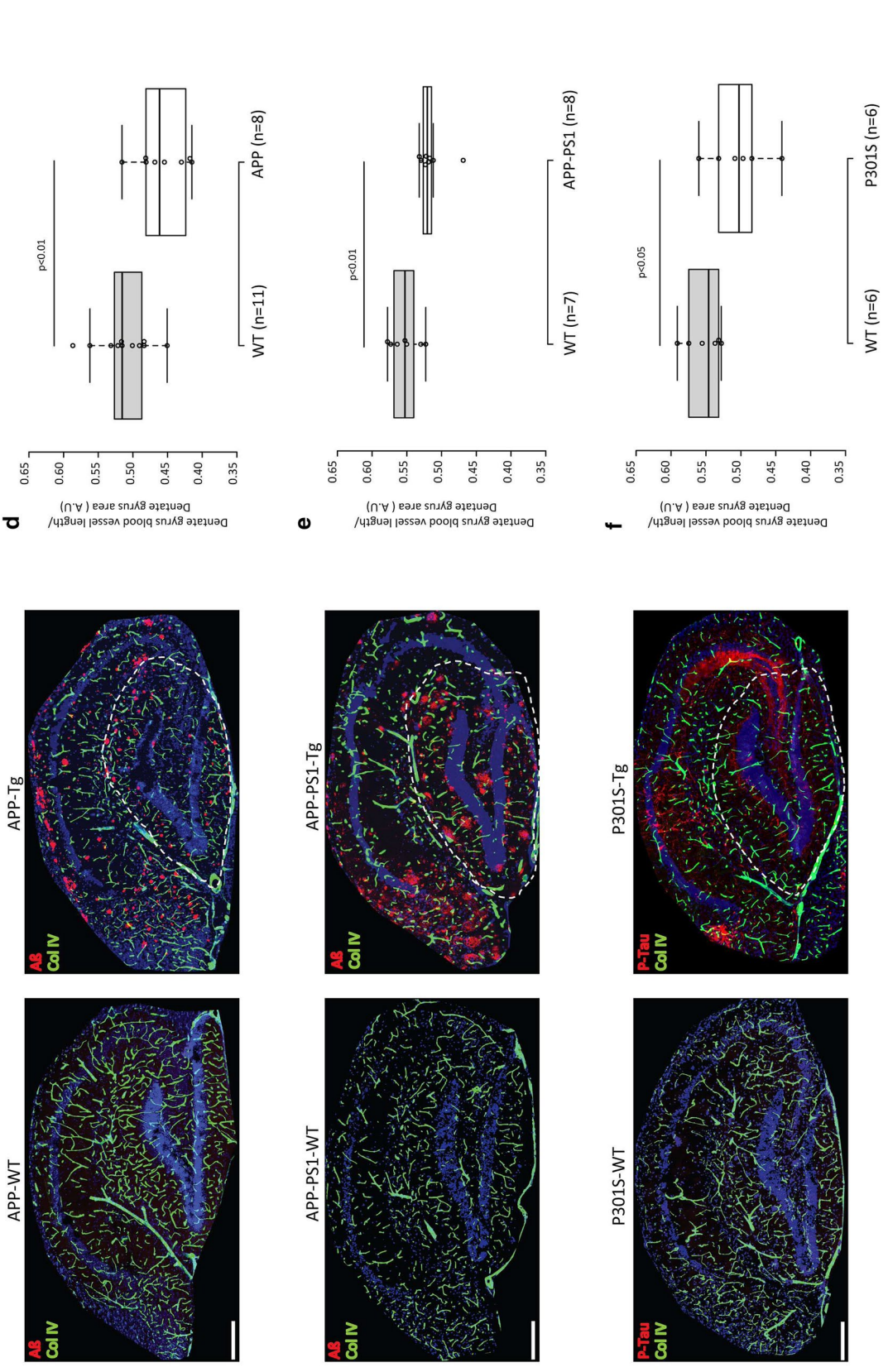

Fig. 7 Blood vessel length is reduced in three mouse models of Alzheimer's disease. Illustration of the accumulation of the two hallmark proteins of Alzheimer's disease amyloid β (**a, b**) and p-Tau (**c**) in the dentate gyrus (dashed lines). Wild-type mice are represented in the left panels while their transgenic littermates are in the right ones (**a–c**). At the age of eight months, Aβ accumulates in TgCRND8 (**a**) and APP-PS1 (**b**) mice whereas p-Tau is overexpressed in P301S mice (**c**). Automated quantification of blood vessels in the dentate gyrus of TgCRND8 (**d**), APP-PS1 (**e**) and P301S (**f**) transgenic mice and their wild-type littermates indicates a reduction of the blood vessel length in all three mouse models of AD (respectively $p < 0.01$, $p < 0.01$ and $p < 0.05$). Horizontal lines in the box represent medians, box limits indicate the 25th and 75th percentiles, whiskers extend 1.5 times the interquartile range from the 25th and 75th percentiles, individual animals are represented as open circles. *p* values of unpaired *t* tests are indicated in the plots for (**d–f**)

protocol with the combination of heat and enzymatic treatment not only helps the efficient staining of vasculature but also enhances the immunohistochemical staining of both amyloid proteins, Aβ and p-Tau. This result is in agreement with the recent finding that a combination of heat and enzymatic treatment was necessary to obtain the most sensitive staining of Aβ on paraffin sections (Kai et al. 2012).

Histological examinations of AD patients and its animal models have shown impairments of microvasculature in specific regions of the brain (Asllani et al. 2008; Buee et al. 1994; Fischer et al. 1990). Functional analysis with MRI has suggested that the cerebral blood flow decreases in the AD mouse brain (Faure et al. 2011; Hebert et al. 2013; Massaad et al. 2010; Poisnel et al. 2012). However, the connection between histological and functional findings needed to be further investigated. For example, Zerbi et al. observed a decrease in the blood volume in APPswe/PS1(dE9) mice but they did not detect any changes in the density of the microvasculature (Zerbi et al. 2013). In our study, the newly established antigen retrieval protocol allowed us to clearly visualize and quantify the vasculature in paraffin-embedded brains. In TgCRND8 APP-transgenic mice, in which vascular damage has been previously described (Paul et al. 2007), and their wild-type littermates we did observe that the length of blood vessels in hippocampus was correlated with the blood flow.

Our findings show that structural vascular dysfunction correlates with hypoperfusion in TgCRND8 mice and suggests that anatomical changes are at least partly responsible for the blood flow decrease. We further show that the morphological changes of the vasculature might be restricted to the capillaries as their diameter is reduced in AD mice and as no change is observed in larger vessels. However, anatomical alteration of the vasculature might not be the unique mechanism involved. Non-anatomical processes such as vasoconstriction have also been described to modulate the cerebral blood flow. Aβ was previously found to directly induce vasoconstriction and reduce cerebral perfusion (Niwa et al. 2001). Furthermore, Aβ was shown to inhibit the production of the vasodilator nitric oxide by decreasing endothelial nitric oxide synthase activity (Lamoke et al. 2015). Such findings strongly suggest that a combination of vasoconstriction and decrease in the blood vessel length might be responsible for the reduction of the blood flow in TgCRND8 mice compared to that in wild-type controls. Nevertheless, Aβ might not be the unique culprit for vasculature alteration in AD patients. In P301S-transgenic mice, we observed a reduction of the vasculature in the dentate gyrus where p-Tau accumulates. This finding is in agreement with the recent discovery that the blood brain barrier is altered in rTg4510 tau-transgenic mice and that Tau depletion is sufficient to prevent it (Blair et al. 2015). The precise mechanism through which Aβ and p-Tau damage endothelial cells still remains unknown. Their accumulation might impair the vasculature directly or by inducing inflammation and/or neurodegeneration or a combination of these factors.

To summarize, we describe a novel simple and robust method to visualize and analyze the brain vasculature on paraffin sections in mouse and human postmortem brains. This methodology offers the possibility to re-examine the brain vasculature in a broader range of archival tissues. In addition, we show that our new method is fully compatible with the detection of glial cells and key markers of AD including Aβ and p-Tau making it a valuable tool to investigate the vasculature both in physiological and pathological conditions. Furthermore, we showed that anatomical alteration of the vasculature directly correlates with the reduction of the blood flow suggesting that the method we developed could be the basis for further identification and characterization of cerebral blood flow alterations in health and disease.

Acknowledgements This work was funded by Grants to K.F. and Y.L. from SNOWBALL, an EU Joint Programme for Neurodegenerative Disease (JPND) (01ED1617B). We thank Professor Frank Kirchhoff for providing us NG2-CreERT2 mice that were crossbred with Rosa26-tdTomato animals. We also thank Elisabeth Gluding, Karin Heintz and Mirjam Müller for excellent technical assistance.

Compliance with ethical standards

Conflict of interest The authors declare that they have no conflict of interest.

References

Asllani I, Habeck C, Scarmeas N, Borogovac A, Brown TR, Stern Y (2008) Multivariate and univariate analysis of continuous arterial spin labeling perfusion MRI in Alzheimer's disease. J Cereb Blood Flow Metabol 28:725–736. https://doi.org/10.1038/sj.jcbfm.9600570

Attems J, Jellinger KA (2014) The overlap between vascular disease and Alzheimer's disease—lessons from pathology. BMC Med 12:206. https://doi.org/10.1186/s12916-014-0206-2

Binnewijzend MA et al (2013) Cerebral blood flow measured with 3D pseudocontinuous arterial spin-labeling MR imaging in Alzheimer disease and mild cognitive impairment: a marker for disease severity. Radiology 267:221–230. https://doi.org/10.1148/radiol.12120928

Blair LJ et al (2015) Tau depletion prevents progressive blood-brain barrier damage in a mouse model of tauopathy. Acta Neuropathol Commun 3:8. https://doi.org/10.1186/s40478-015-0186-2

Bordeleau M, ElAli A, Rivest S (2016) Severe chronic cerebral hypoperfusion induces microglial dysfunction leading to memory loss in APPswe/PS 1 mice. Oncotarget 7:11864–11880. https://doi.org/10.18632/oncotarget.7689

Bouras C et al (2006) Stereologic analysis of microvascular morphology in the elderly: Alzheimer disease pathology and cognitive status. J Neuropathol Exp Neurol 65:235–244. https://doi.org/10.1097/01.jnen.0000203077.53080.2c

Buee L, Hof PR, Bouras C, Delacourte A, Perl DP, Morrison JH, Fillit HM (1994) Pathological alterations of the cerebral microvasculature in Alzheimer's disease and related dementing disorders. Acta Neuropathol 87:469–480

Chishti MA et al (2001) Early-onset amyloid deposition and cognitive deficits in transgenic mice expressing a double mutant form of amyloid precursor protein 695. J Biol Chem 276:21562–21570. https://doi.org/10.1074/jbc.M100710200

Clark PJ, Brzezinska WJ, Puchalski EK, Krone DA, Rhodes JS (2009) Functional analysis of neurovascular adaptations to exercise in the dentate gyrus of young adult mice associated with cognitive gain. Hippocampus 19:937–950. https://doi.org/10.1002/hipo.20543

D'Amico F, Skarmoutsou E, Stivala F (2009) State of the art in antigen retrieval for immunohistochemistry. J Immunol Methods 341:1–18. https://doi.org/10.1016/j.jim.2008.11.007

De Strooper B, Karran E (2016) The cellular phase of Alzheimer's. Dis Cell 164:603–615. https://doi.org/10.1016/j.cell.2015.12.056

Dobre MC, Ugurbil K, Marjanska M (2007) Determination of blood longitudinal relaxation time (T1) at high magnetic field strengths. Magn Reson Imaging 25:733–735. https://doi.org/10.1016/j.mri.2006.10.020

Dorr A et al (2012) Amyloid-beta-dependent compromise of microvascular structure and function in a model of Alzheimer's disease. Brain 135:3039–3050. https://doi.org/10.1093/brain/aws243

Dudvarski Stankovic N, Teodorczyk M, Ploen R, Zipp F, Schmidt MH (2016) Microglia-blood vessel interactions: a double-edged sword in brain pathologies. Acta Neuropathol 131:347–363. https://doi.org/10.1007/s00401-015-1524-y

Faure A et al (2011) Impaired neurogenesis, neuronal loss, and brain functional deficits in the APPxPS1-Ki mouse model of Alzheimer's disease. Neurobiol Aging 32:407–418. https://doi.org/10.1016/j.neurobiolaging.2009.03.009

Fischer VW, Siddiqi A, Yusufaly Y (1990) Altered angioarchitecture in selected areas of brains with Alzheimer's disease. Acta Neuropathol 79:672–679

Franciosi S et al (2007) Pepsin pretreatment allows collagen IV immunostaining of blood vessels in adult mouse brain. J Neurosci Methods 163:76–82. https://doi.org/10.1016/j.jneumeth.2007.02.020

Fries P et al (2012) Comparison of retrospectively self-gated and prospectively triggered FLASH sequences for cine imaging of the aorta in mice at 9.4T. Investig Radiol 47:259–266. https://doi.org/10.1097/RLI.0b013e31823d3eb6

Gama Sosa MA et al (2010) Age-related vascular pathology in transgenic mice expressing presenilin 1-associated familial Alzheimer's disease mutations. Am J Pathol 176:353–368. https://doi.org/10.2353/ajpath.2010.090482

Gama Sosa MA et al. (2014) Selective vulnerability of the cerebral vasculature to blast injury in a rat model of mild traumatic brain injury. Acta Neuropathol Commun 2:67 https://doi.org/10.1186/2051-5960-2-67

Hebert F, Grand'maison M, Ho MK, Lerch JP, Hamel E, Bedell BJ (2013) Cortical atrophy and hypoperfusion in a transgenic mouse model of Alzheimer's disease. Neurobiol Aging 34:1644–1652. https://doi.org/10.1016/j.neurobiolaging.2012.11.022

Herscovitch P, Raichle ME (1985) What is the correct value for the brain–blood partition coefficient for water? J Cereb Blood Flow Metabol 5:65–69. https://doi.org/10.1038/jcbfm.1985.9

Huang SN, Minassian H, More JD (1976) Application of immunofluorescent staining on paraffin sections improved by trypsin digestion Laboratory investigation. J Tech Methods Pathol 35:383–390

Huang W et al (2014) Novel NG2-CreERT2 knock-in mice demonstrate heterogeneous differentiation potential of NG2 glia during development. Glia 62:896–913. https://doi.org/10.1002/glia.22648

Jucker M, Bialobok P, Hagg T, Ingram DK (1992) Laminin immunohistochemistry in brain is dependent on method of tissue fixation. Brain Res 586:166–170

Kai H, Shin RW, Ogino K, Hatsuta H, Murayama S, Kitamoto T (2012) Enhanced antigen retrieval of amyloid beta immunohistochemistry: re-evaluation of amyloid beta pathology in Alzheimer disease and its mouse model. J Histochem Cytochem 60:761–769. https://doi.org/10.1369/0022155412456379

Kim SG, Tsekos NV, Ashe J (1997) Multi-slice perfusion-based functional MRI using the FAIR technique: comparison of CBF and BOLD effects. NMR Biomed 10:191–196

Kloepper J et al (2016) Ang-2/VEGF bispecific antibody reprograms macrophages and resident microglia to anti-tumor phenotype and prolongs glioblastoma survival. Proc Natl Acad Sci USA 113:4476–4481. https://doi.org/10.1073/pnas.1525360113

Kober F et al (2007) MRI follow-up of TNF-dependent differential progression of atherosclerotic wall-thickening in mouse aortic arch from early to. advanced stages. Atherosclerosis 195:e93–e99. https://doi.org/10.1016/j.atherosclerosis.2007.06.015

Kouznetsova E et al (2006) Developmental and amyloid plaque-related changes in cerebral cortical capillaries in transgenic Tg2576 Alzheimer mice. Int J Dev Neurosci 24:187–193. https://doi.org/10.1016/j.ijdevneu.2005.11.011

Lamoke F et al (2015) Amyloid beta peptide-induced inhibition of endothelial nitric oxide production involves oxidative stress-mediated constitutive eNOS/HSP90 interaction and disruption of agonist-mediated Akt activation. J Neuroinflamm 12:84. https://doi.org/10.1186/s12974-015-0304-x

Lee GD, Aruna JH, Barrett PM, Lei DL, Ingram DK, Mouton PR (2005) Stereological analysis of microvascular parameters in a double transgenic model of Alzheimer's disease. Brain Res Bull 65:317–322. https://doi.org/10.1016/j.brainresbull.2004.11.024

Love S, Miners JS (2016) Cerebrovascular disease in ageing and Alzheimer's disease. Acta Neuropathol 131:645–658. https://doi.org/10.1007/s00401-015-1522-0

Massaad CA, Amin SK, Hu L, Mei Y, Klann E, Pautler RG (2010) Mitochondrial superoxide contributes to blood flow and axonal transport deficits in the Tg2576 mouse model of Alzheimer's disease. PloS one 5:e10561 https://doi.org/10.1371/journal.pone.0010561

Mauro A, Bertolotto A, Germano I, Giaccone G, Giordana MT, Migheli A, Schiffer D (1984) Collagenase in the immunohistochemical demonstration of laminin, fibronectin and factor VIII/RAg in nervous tissue after fixation. Histochemistry 80:157–163

Montagne A, Nation DA, Pa J, Sweeney MD, Toga AW, Zlokovic BV (2016) Brain imaging of neurovascular dysfunction in Alzheimer's disease. Acta Neuropathol 131:687–707. https://doi.org/10.1007/s00401-016-1570-0

Mori S, Sternberger NH, Herman MM, Sternberger LA (1992) Variability of laminin immunoreactivity in human autopsy brain. Histochemistry 97:237–241

Muneton-Gomez VC et al (2012) Neural differentiation of transplanted neural stem cells in a rat model of striatal lacunar infarction: light and electron microscopic observations. Front Cell Neurosci 6:30. https://doi.org/10.3389/fncel.2012.00030

Niwa K, Porter VA, Kazama K, Cornfield D, Carlson GA, Iadecola C (2001) A beta-peptides enhance vasoconstriction in cerebral circulation. Am J Physiol Heart Circ Physiol 281:H2417–H2424

Paul J, Strickland S, Melchor JP (2007) Fibrin deposition accelerates neurovascular damage and neuroinflammation in mouse models of Alzheimer's disease. J Exp Med 204:1999–2008. https://doi.org/10.1084/jem.20070304

Poisnel G et al (2012) Increased regional cerebral glucose uptake in an APP/PS1 model of Alzheimer's disease. Neurobiol Aging 33:1995–2005. https://doi.org/10.1016/j.neurobiolaging.2011.09.026

Radde R et al (2006) Abeta42-driven cerebral amyloidosis in transgenic mice reveals early and robust pathology. EMBO Rep 7:940–946. https://doi.org/10.1038/sj.embor.7400784

Shi SR, Key ME, Kalra KL (1991) Antigen retrieval in formalin-fixed, paraffin-embedded tissues: an enhancement method for immunohistochemical staining based on microwave oven heating of tissue sections. J Histochem Cytochem 39:741–748

Soto I et al (2015) APOE stabilization by exercise prevents aging neurovascular dysfunction and complement induction. PLoS Biol 13:e1002279. https://doi.org/10.1371/journal.pbio.1002279

Spitzer M, Wildenhain J, Rappsilber J, Tyers M (2014) BoxPlotR: a web tool for generation of box plots. Nat Methods 11:121–122. https://doi.org/10.1038/nmeth.2811

Vollert CT, Moree WJ, Gregory S, Bark SJ, Eriksen JL (2015) Formaldehyde scavengers function as novel antigen retrieval agents. Sci Rep 5:17322. https://doi.org/10.1038/srep17322

Walchli T et al (2015) Quantitative assessment of angiogenesis, perfused blood vessels and endothelial tip cells in the postnatal mouse brain. Nat Protoc 10:53–74. https://doi.org/10.1038/nprot.2015.002

Whiteus C, Freitas C, Grutzendler J (2014) Perturbed neural activity disrupts cerebral angiogenesis during a postnatal critical period. Nature 505:407–411. https://doi.org/10.1038/nature12821

Yamashita S (2007) Heat-induced antigen retrieval: mechanisms and application to histochemistry. Prog Histochem Cytochem 41:141–200. https://doi.org/10.1016/j.proghi.2006.09.001

Yoshiyama Y et al (2007) Synapse loss and microglial activation precede tangles in a P301S tauopathy mouse model. Neuron 53:337–351. https://doi.org/10.1016/j.neuron.2007.01.010

Zerbi V et al (2013) Microvascular cerebral blood volume changes in aging APP(swe)/PS1(dE9) AD mouse model: a voxel-wise approach. Brain Struct Funct 218:1085–1098. https://doi.org/10.1007/s00429-012-0448-8